X-ray spectral and variability properties of low-mass active galactic nuclei

R. M. Ludlam,[1]★ E. M. Cackett,[1] K. Gültekin,[2] A. C. Fabian,[3] L. Gallo[4] and G. Miniutti[5]

[1]*Department of Physics and Astronomy, Wayne State University, 666 W. Hancock St., Detroit, MI 48201, USA*
[2]*Department of Astronomy, University of Michigan, 500 Church St., Ann Arbor, MI 48109-1042, USA*
[3]*Institute of Astronomy, University of Cambridge, Madingley Rd, Cambridge CB3 0HA, UK*
[4]*Department of Astronomy and Physics, Saint Mary's University, 923 Robie Street, Halifax, NS B3H 3C3, Canada*
[5]*Centro de Astrobiologia (CSIC-INTA), Dep. de Astrofisica, ESAC, PO Box 78, E-28691 Villanueva de la Canada, Madrid, Spain*

ABSTRACT

We study the X-ray properties of a sample of 14 optically selected low-mass active galactic nuclei (AGN) whose masses lie within the range 10^5–2×10^6 $M_{\odot}$ with *XMM–Newton*. Only six of these low-mass AGN have previously been studied with sufficient quality X-ray data, thus, we have more than double the number of low-mass AGN observed by *XMM–Newton* with the addition of our sample. We analyse their X-ray spectral properties and variability and compare the results to their more massive counterparts. The presence of a soft X-ray excess is detectable in all five objects which were not background dominated at 2–3 keV. Combined with previous studies, this gives a total of eight low-mass AGN with a soft excess. The low-mass AGN exhibit rapid, short-term variability (hundreds to thousands of seconds) and long-term variability (months to years). There is a well-known anticorrelation between black hole mass and variability amplitude (normalized excess variance). Comparing our sample of low-mass AGN with this relation we find that all of our sample lie below an extrapolation of the linear relation. Such a flattening of the relation at low masses (below $\sim 10^6$ $M_{\odot}$) is expected if the variability in all AGN follows the same shape power spectrum with a break frequency that is dependent on mass. Finally, we also found two objects that show significant absorption in their X-ray spectrum, indicative of type 2 objects, although they are classified as type 1 AGN based on optical spectra.

Key words: accretion, accretion discs – galaxies: active – galaxies: Seyfert – X-rays: galaxies.

1 INTRODUCTION

Supermassive black holes (with $M \sim 10^6$–10^9 $M_{\odot}$) are thought to be at the centre of all massive galaxies. Black hole (BH) mass measurements have unveiled tight correlations between the host galaxy properties and the BH mass (the *M–L* and *M–σ* relations; e.g. Gültekin et al. 2009, and references therein), and have led to the study of how BHs and galaxies co-evolve (see Kormendy & Ho 2013, for a review). Within this study of co-evolution, there has been much interest in intermediate-mass black holes (IMBHs) with $\sim 10^5$–10^6 $M_{\odot}$, since these objects are both closer to their original primordial mass, as well as existing in smaller, and sometimes bulgeless host galaxies (see Greene 2012, for a review).

An initial sample of 19 IMBH candidates in active galactic nuclei (AGN) was determined by Greene & Ho (2004) based on the Sloan Digital Sky Survey (SDSS) Data Release 1. Using the SDSS Data Release 4 Greene & Ho (2007b) significantly increased the sample size to close to 200 IMBHs. The sample was initially selected

from a search of all AGN that had a broad Hα emission line. The BH masses of this sample were then estimated using the radius–luminosity relation (e.g. Kaspi et al. 2000; Vestergaard 2002; Bentz et al. 2006, 2009, 2013; Vestergaard & Peterson 2006) to obtain an estimate for the radius of the broad line region, and combined with the width of the emission line to estimate the virial BH mass (described in Greene & Ho 2007b). The ~ 200 objects deemed to be within the intermediate-mass range ($< 2 \times 10^6$ $M_{\odot}$) were then selected for further study. A fraction of these (including the objects in our sample) were previously detected by *ROSAT* and noted for their soft X-ray luminosity. While short snapshot X-ray observations of many of these objects have been performed with *Chandra* (Greene & Ho 2007a; Desroches, Greene & Ho 2009; Dong, Greene & Ho 2012), thus far, detailed X-ray spectral fitting has only been performed for a sample consisting of only six IMBHs (Dewangan et al. 2008; Miniutti et al. 2009). Those objects were chosen for their low BH mass, AGN-like spectrum, as well as their high Eddington ratio.

Two well-known low-mass AGN are the spiral galaxy NGC 4395 and the dwarf elliptical galaxy POX 52. Both are seen to be highly variable. A study by Iwasawa et al. (2000) noted that the rapid and

★ E-mail: ef2051@wayne.edu

strong X-ray variability of NGC 4395 was consistent with being a scaled-down Seyfert 1 galaxy. In addition, Moran et al. (2005) observed a number of X-ray properties that make this source unique among type 1 AGN such as the X-ray spectral slope changing from $\Gamma < 1.25$ to $\Gamma > 1.7$ on the time-scale of roughly a year. Thornton et al. (2008) looked at the spectral and variability properties from observations of POX 52 from *XMM–Newton* and *Chandra*, finding variability both on short, 500 s, time-scales and the 9 month time-scale between the two observations.

Another study by Dewangan et al. (2008) performed extensive analysis on both NGC 4395 and POX 52. They characterized their variability, analysed their X-ray spectrum and examined the ultraviolet (UV) emission and optical-to-X-ray spectral index. Short time-scale variability was seen in both NGC 4395 and POX 52. NGC 4395 was found to be the most variable of all AGN that were previously studied. Vaughan et al. (2005) had previously noted that this object's X-ray emission is the most variable of all AGN and exceeds 100 per cent in its fractional variability amplitude. Furthermore, its normalized excess variance was the highest value in comparison with more massive AGN. Both NGC 4395 and POX 52 exhibited broad spectral characteristics of Seyfert 1 galaxies, but NGC 4395 lacked soft excess emission that is a known characteristic to narrow-line Seyfert 1s (NLS1s). From their examination of the data from *XMM–Newton*'s Optical Monitor, Dewangan et al. (2008) were again able to confirm that NGC 4395 and POX 52 resemble NLS1s from their optical-to-X-ray spectral energy distributions.

Miniutti et al. (2009) followed with a study of four IMBHs from the original sample of 19 IMBHs by Greene & Ho (2004): GH 1, GH 8, GH12 and GH 14 (note that when using the ID from Greene & Ho 2007b, these are GH 11, GH 126, GH 171 and GH 181). They focused their research on the X-ray spectral properties, presence of a soft excess and variability of these lesser known IMBHs. The spectra of the IMBHs showed the same shape as the spectra of more massive AGN. They found that, when fitted with a broken power law, the X-ray spectra of their sample were consistent with the photon indices seen in Palomar–Green (PG) quasars in both the hard (2–10 keV) and soft (<2 keV) energies. Moreover, three of the four objects showed the presence of a soft excess in their spectra which is seen in more massive Seyfert 1 galaxies and quasars. This did not shed any more light on the properties and origins of the soft excess emission. However, these objects were extremely X-ray variable when compared to more massive AGN, just like NGC 4395 and POX 52. Their normalized excess variance was higher than the more massive radio-quiet Seyfert 1 galaxies and began to fill in the lower mass portion of the σ^2_{NXS}–M_{BH} relation. The normalized excess variance, σ^2_{NXS}, is a simple measure of the variability amplitude of an object. In the σ^2_{NXS}–M_{BH} relation, as BH mass increases the normalized excess variance decreases. In addition to beginning to fill in the low-mass region, Miniutti et al. (2009) determined that their sample of IMBH accretion properties were similar to those of more massive AGN. This suggests that they are accreting in the same fashion as more massive AGN.

In this work, we analyse 14 additional IMBHs to more than triple the existing sample. The main objectives are to analyse the X-ray spectral properties and characterize the variability of each object. One of the motivations of this study is to see if the conclusions of Miniutti et al. still hold with the addition of a larger sample. In the spectral analysis we will fit the data with various models and look for the presence of a soft excess. We will see how the spectra of this sample compare to more massive AGN, in addition to looking at the variability properties of the sample. We detail our sample in Section 2, describe the observations in Section 3 and our analysis

and results in Section 4. Finally, we discuss our findings and their implications in Section 5.

2 THE SAMPLE

The objects for this sample were based upon the SDSS objects with BH masses estimated to be less than 2×10^6 M$_\odot$ that were published in Greene & Ho (2007b). As part of our *XMM–Newton* AO10 program (PI: Cackett) we observed eight IMBHs. We also searched the archives for other IMBHs with *XMM–Newton* observations longer than 10 ks, leading to a total sample size of 14 objects. Table 1 contains the information on the 14 SDSS objects and their corresponding Greene and Ho (GH) name which were taken from the identification number in table 1 of Greene & Ho (2007b). Those objects that had multiple observations were given a letter that correlates to their event file. We analyse the X-ray spectral properties and characterize the variability of these 14 objects, as well as, compare them to more massive AGN. Note that objects from Greene & Ho (2004) are also in Greene & Ho (2007b), but we only use the ID number from Greene & Ho (2007b) to identify the objects.

3 OBSERVATIONS AND DATA REDUCTION

All observations of our sample were taken with *XMM–Newton* operating in prime full-window imaging mode with either medium or thin filters. Table 1 also includes each object's redshift, galactic column density (N_H) and the exposure time of each European Photon Imaging Camera (EPIC) detector. The exposure times listed are the net exposure times after the data have been filtered for spectral analysis. The X-ray data were reduced by following the step-by-step Science Analysis System (SAS ver. 13.0.0) threads for the EPIC detectors. Good time interval files were created to filter out periods of background flaring for GH 94b, GH 112, GH 116 and GH 181a. For the others, background filtering was either not needed or too much data would have been lost if it was performed. The objects that suffered from high background that was unable to be eliminated are denoted with an asterisk in Table 1. The light curves only use the X-ray data from the EPIC-PN and were binned to 200 s. Depending on the brightness of the image, we used a circular source extraction region with radius 20–30 arcsec.

4 ANALYSIS AND RESULTS

4.1 X-ray spectral analysis

The spectral analysis for each of the objects used data from all three detectors and had 25 counts per energy bin to allow the use of χ^2 minimization. The data were analysed using XSPEC (ver. 12.8.0) in the 0.3–10 keV energy range.

A characteristic of more massive NLS1s is the presence of a soft excess. To examine the presence of a soft excess we first fit a simple power-law model to the 2–10 keV spectrum. We include photoelectric absorption from our own Galaxy with N_H fixed at the Galactic column density towards each object. Many of the PN spectra are background dominated from 2 to 3 keV upwards not allowing for a reliable determination of the 2–10 keV spectral slope. Therefore, for the purposes of looking for the presence of a soft excess, we only examine the five sources which have at least one spectrum that is source dominated at these energies, these are GH 49, GH 78, GH 91, GH 142 and GH 181. After obtaining a fit to the 2–10 keV spectrum, we extrapolate the fit back to the 0.3–2 keV and look for an excess above the model. We find that all five

Table 1. Information on the sample of observed objects.

Object	SDSS name	Event file	Observation date	z	N_H	PN exp	MOS1 exp	MOS2 exp
GH 18	SDSS J022849.51−090153.7	0674810101	17/01/2012	0.0722	3.43	8.7	11.3	11.3
GH 47	SDSS J082443.28+295923.5	0504102001	03/11/2007	0.0254	3.57	19.0	23.0	23.0
GH 49	SDSS J082912.67+500652.3	0303550901	26/04/2006	0.0435	4.05	11.4	16.9	16.9
GH 78	SDSS J094057.19+032401.2	0306050201	30/10/2005	0.0606	3.45	21.9	26.3	26.3
GH 79a*	SDSS J094240.92+480017.3	0201470101	14/10/2004	0.197	1.22	39.5	50.1	50.1
GH 79b		0201470301	13/11/2004			14.4	14.3	14.3
GH 91a	SDSS J102348.44+040553.7	0108670101	05/12/2000	0.0989	2.78	45.7	53.1	53.1
GH 91b		0605540201	13/12/2009			92.6	119	120
GH 91c*		0605540301	08/05/2009			48.0	63.6	63.6
GH 94a	SDSS J103234.85+650227.9	0400570401	06/05/2006	0.0056	1.25	19.5	23.5	23.5
GH 94b		0674810701	10/10/2011			12.8	15.3	16.4
GH 112	SDSS J111644.65+402635.5	0674810401	03/11/2011	0.202	1.72	14.6	17.8	18.3
GH 116	SDSS J112333.56+671109.9	0503600401	22/05/2007	0.055	1.10	17.2	19.4	19.7
GH 138a*	SDSS J115601.13+564923.3	0674810801	29/05/2011	0.118	1.43	4.6	–	–
GH 138b		0674811201	05/11/2011			8.8	11.5	11.5
GH 142a*	SDSS J122342.81+581446.1	0505010101	19/06/2007	0.0143	1.18	7.7	13.8	13.9
GH 142b*		0674810301	03/05/2011			2.6	–	–
GH 142c*		0674810901	20/06/2011			2.3	0.6	0.7
GH 142d*		0674811101	30/10/2011			6.1	8.8	8.8
GH 181a	SDSS J143450.62+033842.5	0305920401	18/08/2005	0.0283	2.51	18.4	26.9	27.5
GH 181b		0674810501	16/08/2011			10.2	13.1	13.1
GH 211a	SDSS J162636.40+350242.0	0505010501	17/08/2007	0.0341	1.44	10.5	13.4	13.4
GH 211b		0505011201	19/08/2007			14.0	17.4	17.4
GH 211c		0674810201	16/08/2011			4.7	7.7	7.7
GH 211d		0674811001	17/01/2012			10.5	13.6	13.4
GH 213	SDSS J163159.59+243740.2	0674810601	28/08/2011	0.0433	3.69	11.5	14.4	14.5

Note. The galactic column density, N_H, is given in the units of 10^{20} cm^{-2}. Net exposure time is given in ks. Observations GH 138a and GH 142b had both EPIC-MOS detectors closed at the time of their observations. * indicates observations that have significant periods of high background that was unable to be eliminated.

Table 2. Spectral parameters for power-law fits to the data between 2 and 10 keV.

Object	Γ_{2-10}	Norm (10^{-5})	χ^2_{2-10}/dof	$\chi^2_{0.3-10}$/dof
GH 18	2.11 ± 0.26	$6.04^{+2.21}_{-1.66}$	0.21	6.17
GH 78	1.82 ± 0.11	13.6 ± 1.9	0.85	12.15
GH 91a	1.96 ± 0.20	$1.90^{+0.53}_{-0.42}$	1.06	8.37
GH 142d	1.58 ± 0.07	$35.2^{+3.24}_{-2.99}$	0.98	3.05
GH 181a	1.63 ± 0.13	3.32 ± 0.60	1.88	5.05
GH 181b	1.79 ± 0.28	4.17 ± 1.77	0.87	2.94

Note. The Galactic column density, N_H, is given in Table 1 and is fixed during the fits. Γ is the power-law index. The normalization of the power law is defined as the photon flux (photons keV^{-1} cm^{-2} s^{-1}) at 1 keV.

sources show a soft excess. We give the 2–10 keV fits in Table 2. Uncertainties on the parameters are quoted at a 1σ confidence level. The χ^2 value over the 0.3–10 keV region is given to indicate the poor fit when extrapolating the model, and hence the presence of a soft excess. We also show the soft excesses for these five objects in Fig. 1. The addition of these five objects to the IMBHs studied previously by Minuitti et al. gives eight objects in this mass range that exhibit a presence of soft excess. The soft excesses all appear reasonably smooth, and no additional components emission or absorption lines are statistically required. The photon indices, Γ, are close to or within the range consistent with those seen in more massive radio-quiet AGN ($1.7 < \Gamma < 2.6$; Dewangan et al. 2008).

We also fit all spectra over the 0.3–10 keV band with an absorbed blackbody plus power-law model, where the blackbody is used to characterize the soft excess. The best-fitting parameters are given in Table 3. The blackbody temperatures were typical of NLS1s in the range of $0.1 < kT < 0.2$ keV (Gierliński & Done 2004). While the high background above 2 keV in many observations has prevented a direct search for a soft excess in many of the objects, indications of a soft excess can be determined from comparing the power-law index in those objects that we have confirmed have a soft excess with the remaining sources. The similar power-law index in most sources may indicate that a soft excess could be present in many of the objects, though better data above 2 keV would be required to confirm this.

GH 47 and GH 94 had a different spectral shape than all the other objects, with a spectral shape resembling that of type 2 AGN. GH 47 and GH 94 were omitted from the spectral fit tables since their spectra cannot be described properly by the same models as the type 1 objects. We describe their spectra in more detail in Section 4.2.

4.2 Type 2 objects

As mentioned above, fits to GH 47 and GH 94 show different spectral shapes compared to the other objects. In the case of GH 47, both a simple power law and a power law plus blackbody model produce extremely poor fits (reduced $\chi^2 > 4.1$ in both cases). For GH 94 (also known as NGC 3259), both spectra are of low quality, with the PN spectra having 250 counts in GH 94a and 200 counts in GH 94b (in the 0.3–10 keV range). Even so, fits with a simple power law are poor (reduced $\chi^2 > 3.9$ in both cases). An acceptable fit can be achieved if fitting a power law plus blackbody model. However, in this case the power-law index for both spectra is $\Gamma < 0$, far from the standard index for type 1 objects. Visual inspection of the spectra
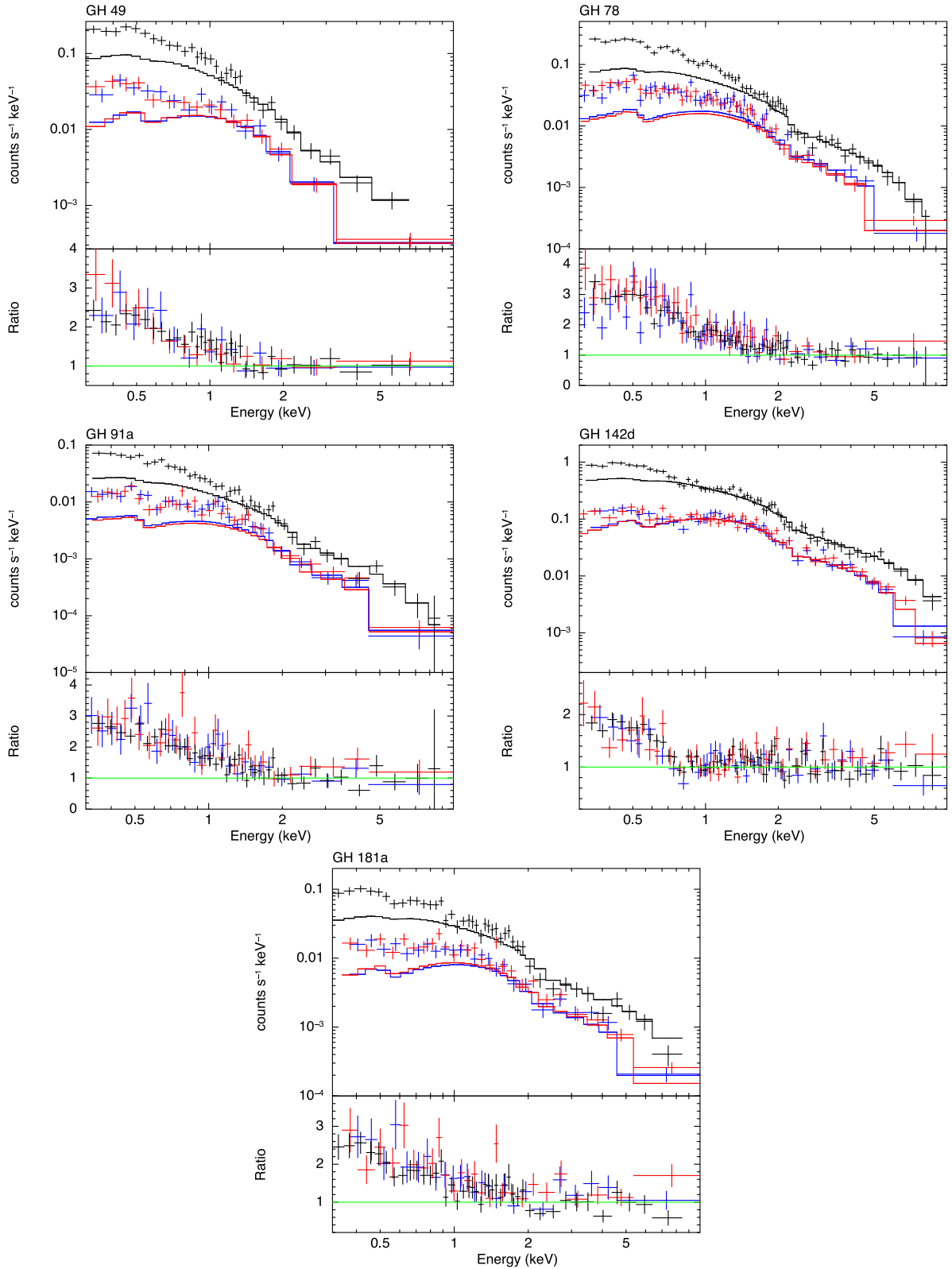
Figure 1. Spectra of the five objects that have a soft excess: GH 49, GH 78, GH 91a, GH 142d and GH 181a. The spectra are fit with a power law above 2 keV only. The panel below each spectrum shows the ratio of the simple power law to the data, showing strong deviations below 2 keV, indicating a soft excess. Blue, red and black points are from the MOS1, MOS2 and PN detectors, respectively.

Table 3. Spectral parameters for fits with a power law plus a blackbody.

Object	kT	Norm (10^{-6})	Γ	Norm (10^{-5})	χ^2/dof	$F_{0.3-10}$	F_{2-10}
GH 18	0.11 ± 0.01	1.81 ± 0.42	2.29 ± 0.11	7.2 ± 0.6	$39.31/60$	3.76 ± 0.12	1.20 ± 0.11
GH 49	0.11 ± 0.01	9.06 ± 1.01	2.39 ± 0.05	43.8 ± 1.4	$269.29/276$	21.1 ± 0.3	6.38 ± 0.25
GH 78	0.12 ± 0.01	3.37 ± 0.57	2.15 ± 0.06	20.2 ± 1.0	$156.55/145$	10.8 ± 0.2	4.17 ± 0.17
GH 79a	0.19 ± 0.06	0.21 ± 0.13	2.98 ± 0.28	2.11 ± 0.46	$108.71/96$	1.12 ± 0.05	0.14 ± 0.06
GH 79b	0.11 ± 0.01	0.92 ± 0.45	2.05 ± 0.51	1.76 ± 0.62	$13.05/13$	1.39 ± 0.17	0.42 ± 0.15
GH 91a	0.12 ± 0.01	0.40 ± 0.12	2.27 ± 0.09	2.75 ± 0.19	$81.62/97$	1.14 ± 0.03	0.48 ± 0.03
GH 91b	0.13 ± 0.01	0.59 ± 0.12	2.39 ± 0.06	3.98 ± 0.17	$216.2/231$	1.98 ± 0.04	0.58 ± 0.04
GH 112	0.12 ± 0.01	2.1 ± 0.5	2.7 ± 0.1	7.4 ± 0.5	$89.28/100$	4.23 ± 0.08	0.67 ± 0.07
GH 116	0.16 ± 0.07	0.27 ± 0.20	2.27 ± 0.35	1.47 ± 0.42	$23.48/17$	0.87 ± 0.10	0.25 ± 0.09
GH 138b	0.15 ± 0.02	1.04 ± 0.43	2.47 ± 0.11	7.81 ± 0.67	$90.19/86$	4.12 ± 0.12	1.01 ± 0.12
GH 142a	0.08 ± 0.01	6.55 ± 0.68	1.69 ± 0.03	42.7 ± 0.8	$377.20/328$	31.3 ± 0.6	17.6 ± 0.5
GH 142b	0.07 ± 0.01	6.8 ± 2.2	1.70 ± 0.08	46.3 ± 2.2	$108.07/106$	33.3 ± 2.1	19.0 ± 2.2
GH 142c	0.10 ± 0.01	6.02 ± 1.04	1.45 ± 0.11	27.2 ± 2.4	$177.26/136$	26.3 ± 2.3	16.4 ± 2.4
GH 142d	0.085 ± 0.005	6.9 ± 0.7	1.58 ± 0.03	36.2 ± 0.8	$278.90/231$	29.7 ± 0.55	17.7 ± 0.6
GH 181a	0.12 ± 0.02	0.53 ± 0.13	1.84 ± 0.07	4.4 ± 0.3	$104.45/91$	2.79 ± 0.08	1.44 ± 0.07
GH 181b	0.12 ± 0.02	0.64 ± 0.19	1.84 ± 0.11	4.3 ± 0.4	$54.68/48$	2.81 ± 0.14	1.41 ± 0.14
GH 211b	0.10 ± 0.03	$0.15^{+0.17}_{-0.06}$	1.28 ± 0.36	0.37 ± 0.11	$4.57/5$	0.46 ± 0.09	0.30 ± 0.07
GH 211d	0.09 ± 0.02	0.52 ± 0.16	1.82 ± 0.1	3.57 ± 0.27	$56.04/59$	2.37 ± 0.15	1.21 ± 0.16
GH 213	0.11 ± 0.03	0.36 ± 0.16	1.97 ± 0.17	2.3 ± 0.3	$15.43/28$	1.29 ± 0.08	0.60 ± 0.09

Note. kT is given in keV. Flux is given in the units of 10^{-13} erg cm^{-2} s^{-1}. N_H is given in Table 1. The normalization of the blackbody component is given as L_{39}/D_{10}^2, where L_{39} is the luminosity of the source in units of 10^{39} erg s^{-1} and D_{10}^2 is the distance to the source in units of 10 kpc. The normalization of the power law is the same as is defined in Table 2.

shows that they resemble type 2 AGN X-ray spectra rather than type 1 spectra. Note that GH 94a was previously analysed by Thornton et al. (2009), who also found the same problems fitting this spectrum with simple models (our results are consistent with theirs). Their best fit was a model including partial covering absorption, similar to the type of model we apply to GH 47 below.

The spectra of GH 94 are too poor to require more complex modelling, however, for GH 47 we fitted a model appropriate for type 2 AGN, consisting of PHABS(POWER LAW+PEXMON+ZPHABS(POWER LAW)). In this model the first absorber is due to Galactic absorption, the first power law is due to scattered emission, the PEXMON component accounts for reflection from the torus and the absorbed power-law accounts for the near Compton-thick absorption of the intrinsic power-law emission from close to the BH. This model provides a significantly improved fit, indicating GH 47 is likely a type 2 AGN. We give the best-fitting spectral parameters in Table 4, and show the best-fitting model along with the PN spectrum in Fig. 2.

4.3 Variability: calculating normalized excess variance

Another objective of studying this sample of low-mass AGN was to characterize their variability and compare them with more massive counterparts. There are well-known anticorrelations between measures of variability and BH mass (see e.g. Ponti et al. 2012; Kelly et al. 2013; McHardy 2013, and references therein). Miniutti et al. (2009) found evidence that the four GH objects they looked at extended the relationship to lower masses. Here, we added 10 GH objects to the low-mass end as well as additional data for one of the objects in Miniutti et al. (2009).

We used PN light curves in the 0.2–10 keV range, binned to 200 s. The light curves exhibit rapid, short time-scale variability (see the two example light curves in Fig. 3). We proceeded to do a comparison of SMBH and IMBH variability by calculating the normalized excess variance, σ^2_{NXS}. The process of calculating the excess variance can be found in Vaughan et al. (2003). The normalized excess variance is just the excess variance divided by the

Table 4. Best-fitting spectral parameters for GH 47.

Component	Parameter	Value
PHABS	N_H (10^{22} cm^{-2})	0.17 ± 0.06
PEXMON	Γ	2.0 ± 0.2
	E_{fold} (keV)	300 (fixed)
	i (°)	60 (fixed)
	Normalization	$(1.2^{+0.8}_{-0.5}) \times 10^{-3}$
POWER LAW (scattered)	Γ	$4.1^{+0.3}_{-0.5}$
	Normalization	$(2.8^{+0.7}_{-0.4}) \times 10^{-5}$
ZPHABS	N_H (10^{22} cm^{-2})	21 ± 3
POWER LAW (intrinsic)	Γ	= pexmon value
	Normalization	$(7.9^{+4.5}_{-1.7}) \times 10^{-4}$
0.5–10 keV flux	(10^{-13} erg cm^{-2} s^{-1})	$9.9^{+1.3}_{-6.3}$
χ^2_ν (dof)		1.48 (128)

Note. The reflection scaling factor is set to -1 to indicate there is no direct component. Abundances were all set to solar values, and z was fixed to 0.0254 in both PEXMON and ZPHABS. The normalization of the PEXMON component is the photon flux at 1 keV. The normalization of the POWER LAW components is defined in Table 2.

square of the average value of the light curve ($\sigma^2_{\text{NXS}} = \sigma^2_{\text{XS}}/\bar{x}^2$). The excess variance is obtained from subtracting expected measurement errors from the standard variance. For the purposes of variability studies we omitted GH 47 and GH 94 from the sample given we find evidence that these objects are type 2 AGN (though see comments on the variability of GH 47 at the end of Section 4.4). For GH 181a, we used light curves that contained the high background periods in order to calculate the excess variance. Filtering for the background would cause multiple gaps of missing data that would have given a misrepresentation of the objects variance.

We chose 10 ks time intervals to calculate the excess variance (note that Miniutti et al. 2009, used 20 ks time intervals) so that we could use data from each of the objects in our sample (the observations were generally shorter than 20 ks). We also recalculated the excess variance for the GH objects in Miniutti et al. (2009) on 10 ks
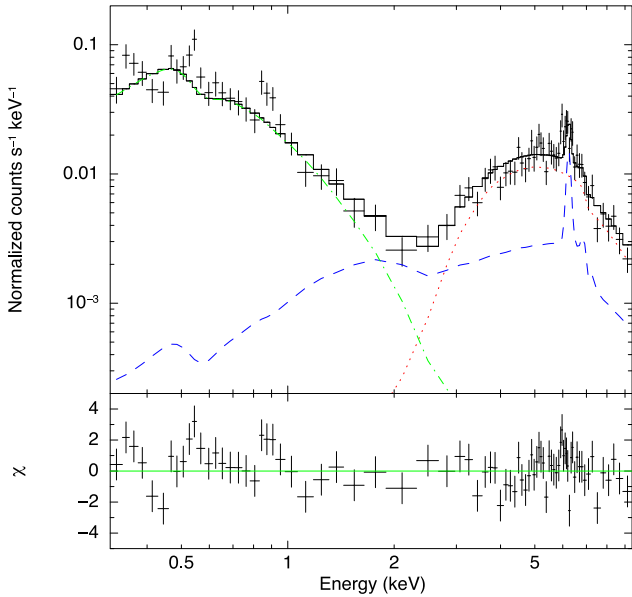
Figure 2. The PN spectrum of GH 47. The solid (black) line indicates the best-fitting type 2 AGN model (see text for details). The blue dashed line indicates the distant reflection (PEXMON) component, the red dotted line is the intrinsic POWER LAW component and the green dash–dotted line is the scattered POWER LAW component. The bottom panel shows the normalized residuals.

time intervals in order to directly compare with the newly analysed GH objects presented here. For those that had observations longer than 10 ks, their data were broken up into 10 ks time intervals and the excess variance was averaged for that object. Segments where the signal-to-noise ratio (S/N) was low and the measured excess variance was less than zero (i.e. when the measurement errors are larger than the standard variance) were not included in the averaging. Table 5 gives the normalized excess variances for all GH objects analysed here. GH 79 had a highly unconstrained value, and thus we do use it here.

The statistical uncertainty in the normalized excess variance was calculated using the formulae in Vaughan et al. (2003), who investigate the error in the measured excess variance through Monte Carlo simulations. Importantly, from the Monte Carlo simulations they find that the normalized excess variance is an unbiased estimator of the intrinsic variance, even when the S/N is relatively low. In addition to the statistical uncertainty there is also a stochastic uncertainty as the variance of the light curve depends upon when it is observed. Vaughan et al. (2003) also examine this in detail, and we follow the Ponti et al. (2012) method for including this in the total uncertainty in the normalized excess variance (see their appendix A, though we calculate the 1σ error rather than the 90 per cent confidence level). Note that in almost all cases the stochastic uncertainty completely dominates over the statistical uncertainty.

4.4 Variability and black hole mass

The most comprehensive study to date of BH mass versus normalized excess variance was performed by Ponti et al. (2012), where they calculated the normalized excess variance for a large sample of variable AGN observed by *XMM–Newton*. Ponti et al. (2012) calculate the normalized excess variance in the 2–10 keV band. However, in our sample of GH objects many of the sources are background dominated above 2 keV. In order to maximize the number of sources
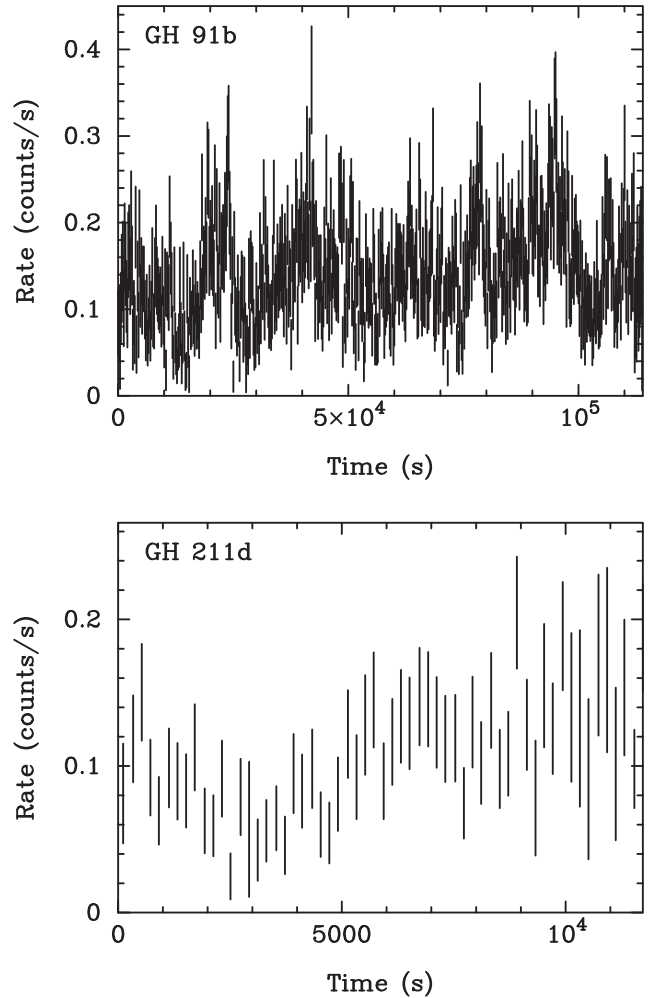

Figure 3. 0.2–10 keV background-subtracted light curves from two objects in our sample, GH 91b (top) and GH 211d (bottom).

we could obtain a measurement of the normalized excess variance we therefore used light curves in the 0.2–10 keV range. We cannot directly compare our results with those of Ponti et al. (2012). We therefore calculated the normalized excess variance for the sample of Seyfert 1s used in Miniutti et al. (2009) using 0.2–10 keV light curves and 200 s bins (see Table 6). We note that from the Miniutti et al. (2009) sample we removed two sources (IC 4329A and PG 1211+143) as they are determined to have low-quality BH mass estimates by Peterson et al. (2004). A third source, Fairall 9, had a very large stochastic uncertainty in the normalized excess variance, and so we do not use that object here either.

In order to make the most robust comparison between normalized excess variance and BH mass we updated the GH BH masses using the latest scaling relation involving the Hα luminosity and full width at half-maximum (FWHM) from Reines, Greene & Geha (2013) (their equation 5), using $\epsilon = 1.0775$. Reines et al. (2013) use the most recent R–L scaling relation from Bentz et al. (2013) following the approach of Greene & Ho (2004, 2007b). $\epsilon = 1.0775$ corresponds to the mean virial factor $\langle f \rangle = 4.31 \pm 1.05$ determined by Grier et al. (2013) from recalibrating reverberation masses to the M–σ relation, and using $\epsilon = f/4$ from assuming that $\sigma = V_{\rm FWHM}/2$ (Onken et al. 2004). Table 5 gives the updated GH BH masses. Note that the updated masses are systemically slightly larger than the original GH masses, but it is not a large effect.

Table 5. BH mass and excess variance for the GH objects.

Object	$\log(M_{\mathrm{BH}}/M_{\odot})$	$\log(\sigma^2_{\mathrm{NXS}})$	$\log(L_{\mathrm{bol,X}})$	$L_{\mathrm{bol,X}}/L_{\mathrm{Edd}}$	$\log(L_{\mathrm{bol,H\alpha}})$	$L_{\mathrm{bol,H\alpha}}/L_{\mathrm{Edd}}$	$L_{\mathrm{bol,X}}/L_{\mathrm{bol,H\alpha}}$
GH 11	6.26	-1.36 ± 0.51	43.71	0.22	43.89	0.34	0.65
GH 18	5.52	-1.55 ± 0.41	43.29	0.43	42.98	0.23	2.09
GH 49	6.03	-1.40 ± 0.30	43.57	0.28	43.61	0.30	0.93
GH 78	6.26	-1.72 ± 0.14	43.71	0.22	43.90	0.34	0.65
GH 91	5.78	-1.28 ± 0.55	43.12	0.18	43.47	0.39	0.45
GH 112	5.88	-1.34 ± 1.05	44.11	1.36	43.58	0.40	3.44
GH 116	5.39	-0.82 ± 0.88	42.18	0.049	42.56	0.12	0.41
GH 126	6.20	-1.80 ± 0.45	43.78	0.30	44.00	0.50	0.60
GH 138	6.03	-1.36 ± 0.46	43.52	0.24	43.56	0.27	0.90
GH 142	5.78	-1.61 ± 1.01	42.93	0.11	42.91	0.11	1.04
GH 171	6.29	-1.82 ± 0.49	44.11	0.53	44.03	0.43	1.09
GH 181	5.86	-0.79 ± 0.75	42.36	0.025	42.94	0.096	0.26
GH 211	5.82	-0.91 ± 1.09	42.15	0.017	43.30	0.24	0.071
GH 213	5.90	-1.41 ± 1.63	42.37	0.023	43.37	0.24	0.10

Note. $L_{\mathrm{bol,X}}$ is the bolometric luminosity given in erg s^{-1} based on the 2–10 keV flux, applying the bolometric correction of Marconi et al. (2004). $L_{\mathrm{bol,H\alpha}}$ is the bolometric luminosity given in erg s^{-1} based on the Hα luminosity from Greene & Ho (2007b) and is given here for comparison. GH names refer to Greene & Ho (2007b). Note that GH 11, GH 126, GH 171 and GH 181 listed here are sometimes alternatively known as GH 1, GH 8, GH12 and GH14 when using the Greene & Ho (2004) rather than Greene & Ho (2007b) ID numbers.

Table 6. Mass and variability for the Seyfert 1 sample.

Name	$\log(M_{\mathrm{BH}}/M_{\odot})$	f_{Edd}	$\log \sigma^2_{\mathrm{NXS}}$	Mass reference
1H 0707−495	6.37	0.17	-1.14 ± 0.30	Zhou & Wang (2005)
Ark 120	7.98	0.25	-4.05 ± 1.36	Grier et al. (2013)
Ark 564	6.65	1.07	-1.70 ± 0.38	Botte et al. (2004)
HE 1029−1401	9.31	0.067	-3.30 ± 0.69	McLure & Dunlop (2001)
IRAS 13224−3809	6.76	0.16	-0.94 ± 0.37	Zhou & Wang (2005)
I Zw 1	7.45	0.76	-2.20 ± 0.53	Botte et al. (2004)
MCG−6−30−15	6.87	0.090	-1.58 ± 0.45	McHardy et al. (2005)
Mrk 110	7.32	0.99	-3.75 ± 0.86	Grier et al. (2013)
Mrk 335	7.03	0.26	-2.00 ± 0.69	Peterson et al. (2004)
Mrk 478	7.55	0.34	-2.04 ± 0.43	Grupe et al. (2004)
Mrk 509	7.95	0.39	-3.98 ± 0.53	Grier et al. (2013)
Mrk 766	6.10	0.91	-1.75 ± 0.33	Grier et al. (2013)
Mrk 841	8.24	0.053	-2.99 ± 0.90	Grupe et al. (2004)
MS 2254−36	6.89	0.22	-1.99 ± 0.49	Grupe et al. (2004)
NGC 3783	7.26	0.090	-2.63 ± 0.44	Grier et al. (2013)
NGC 4051	6.32	6.9×10^{-3}	-0.99 ± 0.35	Grier et al. (2013)
NGC 4151	7.65	0.013	-3.34 ± 0.55	Grier et al. (2013)
NGC 4395	5.44	3.5×10^{-3}	-0.74 ± 0.43	Peterson et al. (2005)
NGC 4593	6.94	0.11	-2.43 ± 0.34	Grier et al. (2013)
NGC 5548	7.76	0.088	-3.54 ± 0.76	Grier et al. (2013)
NGC 7469	7.30	0.16	-3.08 ± 0.33	Grier et al. (2013)
Ton S180	7.00	0.94	-1.93 ± 0.33	Grupe et al. (2004)
WAS 61	6.96	0.55	-2.38 ± 0.39	Grupe et al. (2004)

We also use the most up-to-date masses for the Seyfert 1 sample. For the objects whose masses have been measured directly from reverberation mapping, we use the most recent masses from Grier et al. (2013), where available. For those reverberation mapped AGN not in Grier et al. (2013), we use the Peterson et al. (2004) virial product to calculate the BH mass using the Grier et al. (2013) f value, except for NGC 4395 where we use the Peterson et al. (2005) virial product. The other AGN have their masses estimated via reverberation-based scaling relations, using the 5100 Å luminosity to estimate the broad line region radius (from the R–L relation) and combining the radius with the FWHM of the Hβ broad emission line in order to get the mass. We obtained the $\lambda L_\lambda(5100$ Å$)$ and

FWHM(Hβ) values for each object from the literature, and used the most recent R–L relation of Bentz et al. (2013) in order to estimate R_{BLR} (their 'clean' fit, also used in determining the Hα relations of Reines et al. 2013). Of all the sources, for only two could we not find literature values for $\lambda L_\lambda(5100$ Å$)$ and FWHM(Hβ). For those sources (1H 0707−495 and IRAS 13224−3809) we use literature values for BH mass estimates. All masses for the Seyfert 1 sample are given in Table 6.

We compare the GH objects to the Seyfert 1 sample in order to see whether the anticorrelation between BH mass and normalized excess variance holds at low mass, as suggested from the four GH objects studied by Miniutti et al. (2009). Fitting the Seyfert 1 sample
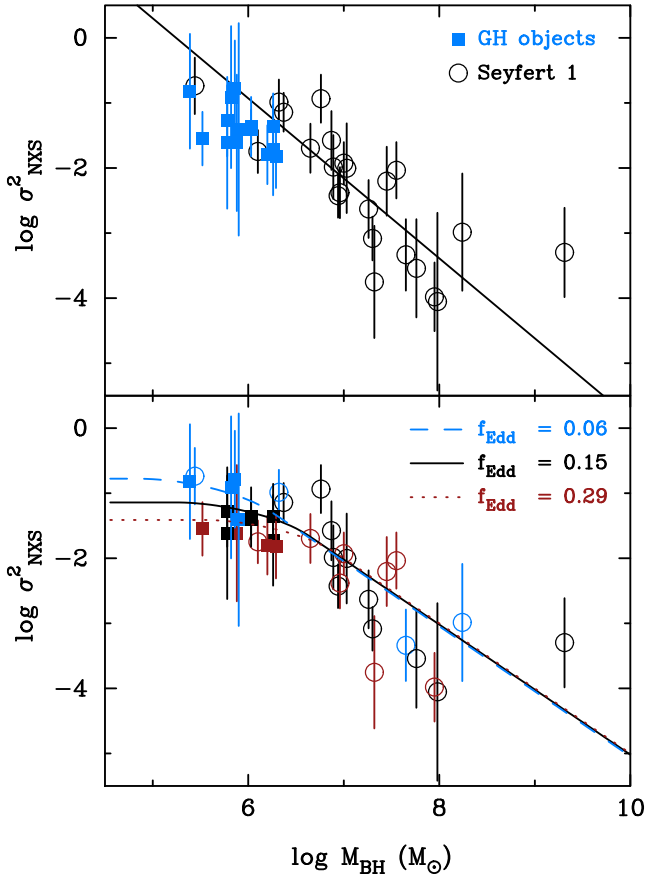
Figure 4. Normalized excess variance (σ^2_{NXS}) versus BH mass. Top: the black open circles indicate the sample of Seyfert 1 objects, while the blue filled squares indicate the GH objects. The line is the best linear-bisector fit to the Seyfert 1 sample. Bottom: colours of the data points indicate the range of f_{Edd}, with blue indicating $f_{\mathrm{Edd}} < 0.06$, black $0.06 \leq f_{\mathrm{Edd}} \leq 0.29$ and red $f_{\mathrm{Edd}} > 0.29$. The lines are plotted for $f_{\mathrm{Edd}} = 0.06$ (dashed blue), $f_{\mathrm{Edd}} = 0.15$ (solid black) and $f_{\mathrm{Edd}} = 0.29$ (dotted red). These are the 33rd, 50th and 67th percentile of the f_{Edd} distribution of the sample.

with a simple linear relation (using a linear bisector as in Ponti et al. 2012), we find

$$\log\left(\sigma^2_{\mathrm{NXS}}\right) = (-1.23 \pm 0.22)\log\left(\frac{M_{\mathrm{BH}}}{10^7\,\mathrm{M_\odot}}\right) - (2.15 \pm 0.12) \tag{1}$$

for the sample we are using. Note that this is consistent with the similar fits in Ponti et al. (2012) where the excess variance in calculated in the 2–10 keV band.

In the top panel of Fig. 4 we compare the normalized excess variances of the GH BHs (blue squares) to those from the Seyfert 1 sample (black circles). Broadly speaking, it appears that the GH objects show that this relation extends to low masses. However, we note that all 14 of the GH objects lie below the best-fitting line quoted above. If measurements are equally likely to lie above and below the line, this would happen 0.012 per cent of the time (using a two-sided binomial test), and hence we can rule out an extrapolation of the linear relation to these data at 3.8σ confidence.

Such an offset for low-mass objects is expected if all AGN have the same underlying power spectrum with a slope of -2 at high frequencies that breaks to a slope of -1 at low frequencies, with a break frequency, ν_{br}, that scales with mass (Papadakis 2004; O'Neill et al.

2005; González-Martín et al. 2011; Ponti et al. 2012; Kelly et al. 2013). In calculating the excess variance we only probe time-scales between the binning time of the light curves (200 s here) and the length of the light-curve segments (10 ks here). For BHs with masses significantly above $10^6\,\mathrm{M_\odot}$, the break frequency is low enough that it occurs on time-scales longer than the 10 ks light-curve length. The light curves are therefore just sampling variability occurring on the part of the power spectrum with a slope of -2. However, once masses get below a few times $10^6\,\mathrm{M_\odot}$, ν_{br} corresponds to a time-scale shorter than the length of the light curve, and we start to also probe the power spectrum with a slope of -1. This changes the expected BH mass–excess variance relation, which should flatten from a slope of -1 at higher masses to a slope of 0 below $\sim 10^6\,\mathrm{M_\odot}$ (Papadakis 2004; O'Neill et al. 2005; González-Martín et al. 2011; Ponti et al. 2012). Having all 14 GH objects lie below a simple linear relation determined from more massive objects is therefore consistent with expectations of AGN having a universal power spectrum that scales with BH mass.

We proceed to fit the BH mass–excess variance relation with models that assume a universal power spectrum. We follow the prescription of González-Martín et al. (2011) as modified by Ponti et al. (2012) to allow for further dependencies on mass accretion rate. We describe the model below. Note that in previous work, authors tend to refer to the mass accretion rate as a fraction of the Eddington ratio, $\dot{m}_{\mathrm{Edd}}$, which is usually determined from $L_{\mathrm{bol}}/L_{\mathrm{Edd}}$. We prefer to refer to this as the Eddington fraction, f_{Edd}, since, there is a correction for efficiency to go from L_{bol} to $\dot{m}$ that is not included when using $\dot{m}_{\mathrm{Edd}} = L_{\mathrm{bol}}/L_{\mathrm{Edd}}$.

First, we assume that the break frequency scales with both M_{BH} and f_{Edd} (McHardy et al. 2004, 2006; Uttley & McHardy 2005; Körding et al. 2007). As shown by McHardy et al. (2006):

$$\nu_{\mathrm{br}} = 0.003\,f_{\mathrm{Edd}}(M_{\mathrm{BH}}/10^6\,\mathrm{M_\odot})^{-1}\,\mathrm{Hz}. \tag{2}$$

Following González-Martín et al. (2011) we then calculate σ^2_{NXS} using

$$\sigma^2_{\mathrm{NXS}} = \begin{cases} C\nu_{\mathrm{br}}\left(\nu_{\min}^{-1} - \nu_{\max}^{-1}\right) & (\text{if }\nu_{\mathrm{br}} < \nu_{\min}), \\ C\left[\ln\left(\frac{\nu_{\mathrm{br}}}{\nu_{\min}}\right) - \frac{\nu_{\mathrm{br}}}{\nu_{\max}} + 1\right] & (\text{if }\nu_{\min} < \nu_{\mathrm{br}} < \nu_{\max}), \\ C\ln\left(\frac{\nu_{\max}}{\nu_{\min}}\right) & (\text{if }\nu_{\mathrm{br}} > \nu_{\max}). \end{cases} \tag{3}$$

Ponti et al. (2012) argue that the presence of objects with similar mass but quite different values of σ^2_{NXS} suggests a dependence of the normalization of the power spectrum on f_{Edd}. We therefore parametrize our model similarly:

$$C = Af_{\mathrm{Edd}}^{-\beta}, \tag{4}$$

which is referred to as Model B by Ponti et al. (2012). In fitting this to the sample, then, A and β are the free parameters, while M_{BH}, σ^2_{NXS} and f_{Edd} are the observables.

To fit this model we need to determine the bolometric luminosity of the objects in our sample in order to estimate f_{Edd}. Ponti et al. (2012) use the bolometric correction of Marconi et al. (2004) in order to go from 2 to 10 keV X-ray luminosity to bolometric luminosity. For consistency, we therefore also take this same approach to determine the bolometric luminosities of the GH objects and Seyfert 1 sample. In Table 5 we give the bolometric luminosity based on the average 2–10 keV luminosity of each GH object in our sample, along with the Eddington fraction. We calculate X-ray luminosities assuming $H_0 = 70\,\mathrm{km\,s^{-1}\,Mpc^{-1}}$, $\Omega_{\mathrm{m}} = 0.3$, $\Omega_\Lambda = 0.7$. For comparison, we also give the bolometric luminosity based on the Hα luminosity (taken from Greene & Ho 2007b), the associated Eddington fraction and the ratio of the Eddington fraction based on
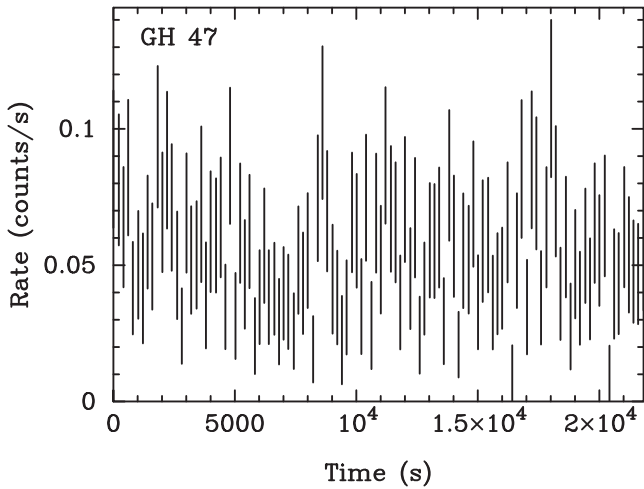
Figure 5. 0.2–2 keV background-subtracted light curve of the type 2 object GH 47.

the X-ray luminosity to the Eddington fraction based on the Hα luminosity. Eddington fractions for our Seyfert 1 sample are given in Table 6 and are also obtained from using the bolometric correction of Marconi et al. (2004) on the 2–10 keV unabsorbed fluxes. We obtain the 2–10 keV unabsorbed fluxes through spectral fitting of all observations in our sample.

We fitted the above model for the mass–variability relation to the full sample of objects using the X-ray determined values of f_{Edd}. We assume that σ^2_{NXS} is the dependent variable in the fits. We determine the uncertainties in A and β from 10 000 Monte Carlo simulations, and take the median of the distribution as the best-fitting values and the 68 per cent interval as our uncertainties. We get a best fit with $A = (3.5 \pm 1.0) \times 10^{-3}$, $\beta = 0.94 \pm 0.13$.

To graphically demonstrate the best fit (we cannot simply plot a best-fitting line since each object has a different f_{Edd}), we split the sample into three subsamples based on their f_{Edd}. In the bottom panel of Fig. 4, the objects in the bottom third of the distribution ($f_{Edd} < 0.06$) are shown in blue, those in the middle third are shown in black ($0.06 \leq f_{Edd} \leq 0.29$) and those in the upper third ($f_{Edd} > 0.29$) are shown in red. The three lines represent the boundaries between these regions and the median value. It can clearly be seen that above approximately 10^6 M$_\odot$ all the models show approximately the same relation. Below this mass the models all flatten and there is a small dispersion between the lowest and highest f_{Edd} models, as expected by the model.

Finally, we consider the variability in the type 2 object, GH 47. We would expect the variability of the soft emission (dominated by the scattered power-law component) to have little variability, and that is what we find. In Fig. 5 we show the 0.2–2 keV light curve of GH 47. The normalized excess variance across the 0.2–10 keV band (in order to compare to the other GH objects) is $\log \sigma^2_{NXS} = -2.9$, significantly smaller than all the other GH objects, as would be expected if it is a type 2 object.

4.5 Long time-scale variability

In addition to short time-scale variability (shorter than the length of observations), there is also variability exhibited by our sample over a long period of time (between observations: months–years). The fluxes originally detected by the *ROSAT* All Sky Survey (RASS) are listed in Table 7. The fluxes from the time that they were observed by *XMM–Newton* are listed in the following column. The difference

Table 7. Flux comparison in the 0.5–2.0 keV range.

Object	*ROSAT*	Date of *XMM* obs	*XMM–Newton*
GH 18	2.2 ± 0.8	17/01/2012	1.80 ± 0.04
GH 78	10.7 ± 3.7	30/10/2005	4.94 ± 0.06
GH 112	3.6 ± 2.1	03/11/2011	2.11 ± 0.29
GH 138a	2.3 ± 1.9	29/05/2011	0.55 ± 0.08
GH 138b		05/11/2011	2.03 ± 0.04
GH 142a	2.3 ± 1.5	19/06/2007	10.4 ± 0.1
GH 142c		03/05/2011	10.8 ± 0.3
GH 142d		20/06/2011	7.56 ± 0.22
GH 142e		30/10/2011	9.13 ± 0.09
GH 181a	2.4 ± 2.0	18/08/2005	1.07 ± 0.02
GH 181b		16/08/2011	1.09 ± 0.03
GH 211a	5.2 ± 3.3	17/08/2007	0.092 ± 0.013
GH 211b		19/08/2007	0.12 ± 0.01
GH 211c		16/08/2011	0.32 ± 0.02
GH 211d		17/01/2012	0.87 ± 0.02
GH 213	2.2 ± 0.7	28/08/2011	0.53 ± 0.02

Note. Flux is given in units of 10^{-13} erg cm^{-2} s^{-1}. There is a significant change in the flux between the time *ROSAT* and *XMM–Newton* took their observations. *ROSAT* detection flux values are obtained from table 4 in Greene & Ho (2007b).

in the observed fluxes over these extended time periods between observation shows long-term variability, not just between *ROSAT* and *XMM–Newton* observations, but also between individual *XMM–Newton* pointings. Several objects' fluxes have changed by a factor of 4 between the time that *ROSAT* and *XMM–Newton* had observed them. Between the four observations of GH 211 alone the flux changed by a factor of almost 10.

5 DISCUSSION

Using observations with *XMM–Newton*, we have determined the X-ray spectral and variability properties of a sample of 14 AGN estimated to have masses $<2 \times 10^6$ M$_\odot$ by Greene & Ho (2007b).

Of all the sources examined here, five had spectra that were not background dominated at 2–3 keV. When fitting the spectra of these five objects from 2 to 10 keV with a simple absorbed power law and extrapolating back to the 0.3–2 keV range, we found a soft excess was present in all five objects. The power-law indices are close to or within the range consistent with those seen in more massive radio-quiet AGN ($1.7 < \Gamma < 2.6$; Dewangan et al. 2008). When fitting the soft excess with a blackbody component, the blackbody temperatures were found to be consistent with 0.1–0.2 keV, as is typically seen in type 1 AGN (Gierliński & Done 2004). Combining our results with the previous findings of Miniutti et al. (2009), we find that a total of eight GH objects are known to show a soft excess.

The nature of the soft excess is still uncertain, though the fact that the characteristic blackbody temperature is constant over a wide range in BH mass suggests an atomic origin. Reflection of hard X-rays off the accretion disc can successfully fit the soft excess (Crummy et al. 2006; Walton et al. 2013), but may not be sufficient or required in every instance (Lohfink et al. 2012; Matt et al. 2014). An alternative suggestion for the origin of the soft excess involves optically thick Comptonized disc emission (Done et al. 2012), which should be most prominent in lower mass objects due to their hotter discs. The soft excesses present in a significant fraction of the low-mass AGN studied here would be a good test of these models if a particularly high S/N spectrum was obtained, especially because the Done et al. (2012) model should be most prominent in lower mass objects. We note that the spectra are all relatively smooth

at low energies, with no spectrum statistically requiring additional emission lines. In the reflection origin for the soft excess, this would imply these objects are rapidly spinning (in order to smooth out reflection features).

Two objects in the sample, GH 47 and GH 94, both show spectra that cannot be simply fit by a power law plus a blackbody. Those objects displayed spectra consistent with being classed as type 2 AGN. Moreover, the light curve of GH 47 has significantly less variability than the other GH objects, as expected from our type 2 classification. While these two objects were initially classed as type 1 AGN optically (based on the presence of a broad Hα line), they appear to be type 2 from X-ray observations. We note, however, that a follow-up Magellan observation of GH 47 by Xiao et al. (2011) found that the peak amplitude of the Hα line was not as significant as other type 1 AGN in comparison to the rms deviation of the continuum-subtracted spectrum. These authors therefore flagged this object as having only a possible broad Hα line which makes the optical type 1 classification insecure. Additionally, Thornton et al. (2009) classify GH 94 as a type 2 based on the weak broad Hα emission line. Thus, the type 1 optical classification of both these objects is questionable. However, if these two objects are type 1 AGN optically yet type 2 in the X-ray regime, then this adds to the sample of AGN where optical and X-ray classifications differ (e.g. see the discussion in Matt 2002).

We also studied the X-ray variability properties of these GH objects. A comparison of the fluxes of the objects from the RASS and multiple *XMM–Newton* observations shows long-term variability (time-scale of months to years). We also detected significant short-term variability (hundreds to thousands of seconds) during the observations. It has long been known that short time-scale variability amplitude scales inversely with BH mass (see Ponti et al. 2012; Kelly et al. 2013, and references therein). A similar inverse scaling holds even when fitting for the overall normalization of the X-ray power spectrum (McHardy 2013). This is expected based simply on the fact that the size scale for the system scales linearly with BH mass (the gravitational radius, $r_g = GM/c^2$). If this is the dominant effect, then more massive BHs have bigger accretion discs and thus will be less variable on shorter time-scales. Such inverse scaling with BH mass has been observed when using either the normalized excess variance (e.g. Ponti et al. 2012) or the rate of stochastic variability power (Kelly et al. 2013) as a measure of the variability amplitude. The scatter in the relation is also quite small (∼0.3 dex), indicating that measures of variability are a promising way to estimate BH masses.

No study of variability amplitude versus mass has included a significant number of BHs at the low-mass end, thus it was not clear to what extent this relation can be extrapolated to lower masses, although, Miniutti et al. (2009), who studied four GH objects, found that they appeared to extend the relation to lower masses. Here, we compare a total of 14 GH objects with a sample of 23 Seyfert 1s. We find that the GH objects do have high normalized excess variance values, as expected for lower mass AGN, but that all 14 objects lie below the best-fitting log-linear relation fit to more massive Seyfert 1s, ruling out a simple extrapolation of that relation at 3.8σ confidence. This is expected in the case of a universal power spectrum with a break frequency that scales with mass (Papadakis 2004; O'Neill et al. 2005; González-Martín et al. 2011; Ponti et al. 2012; Kelly et al. 2013). For low-mass objects the break frequency becomes larger than the frequencies probed by the light curve. We proceed to fit the BH mass versus excess variance relation with models taking this into account, and find that the data support that these are low-mass objects displaying variability that follows a

universal power spectrum, supporting previous work showing the scaling of the power spectrum between BH X-ray binaries and AGN (McHardy et al. 2006).

As discussed by previous authors (e.g. Ponti et al. 2012; Kelly et al. 2013), because the BH mass–excess variance relation flattens off for masses below approximately 10^6 M$_\odot$ it cannot be used to directly measure the mass of objects below this value. However, the fact that we see the relation flatten demonstrates that the AGN have masses below approximately this value. In order to use variability to independently estimate the BH masses of these objects it would require using a method such as the rate of stochastic variability power developed by Kelly et al. (2013). However, it is unclear as to whether the quality of data from the *XMM–Newton* observations would be sufficient enough for this kind of analysis.

Not included in the model of how excess variance changes with BH mass is the effect of BH spin. The change in the location of the innermost stable circular orbit between a non-rotating and maximally rotating BH should have an effect on the variability properties and will add scatter to the BH mass–excess variance relation.

In summary, the spectral and variability properties of the low-mass AGN are similar to more massive Seyferts, with the definite existence of a soft excess in some low-mass AGN, and variability amplitude that is consistent with there being a universal power spectrum for all AGN.

REFERENCES

Bentz M. C., Peterson B. M., Pogge R. W., Vestergaard M., Onken C. A., 2006, ApJ, 644, 133
Bentz M. C., Peterson B. M., Netzer H., Pogge R. W., Vestergaard M., 2009, ApJ, 697, 160
Bentz M. C. et al., 2013, ApJ, 767, 149
Botte V., Ciroi S., Rafanelli P., Di Mille F., 2004, AJ, 127, 3168
Crummy J., Fabian A. C., Gallo L., Ross R. R., 2006, MNRAS, 365, 1067
Desroches L.-B., Greene J. E., Ho L. C., 2009, ApJ, 698, 1515
Dewangan G. C., Mathur S., Griffiths R. E., Rao A. R., 2008, ApJ, 689, 762
Done C., Davis S. W., Jin C., Blaes O., Ward M., 2012, MNRAS, 420, 1848
Dong R., Greene J. E., Ho L. C., 2012, ApJ, 761, 73
Gierliński M., Done C., 2004, MNRAS, 349, L7
González-Martín O., Papadakis I., Reig P., Zezas A., 2011, A&A, 526, A132
Greene J. E., 2012, Nat. Commun., 3, 1304
Greene J. E., Ho L. C., 2004, ApJ, 610, 722
Greene J. E., Ho L. C., 2007a, ApJ, 656, 84
Greene J. E., Ho L. C., 2007b, ApJ, 670, 92
Grier C. J. et al., 2013, ApJ, 773, 90
Grupe D., Wills B. J., Leighly K. M., Meusinger H., 2004, AJ, 127, 156
Gültekin K. et al., 2009, ApJ, 698, 198
Iwasawa K., Fabian A. C., Almaini O., Lira P., Lawrence A., Hayashida K., Inoue H., 2000, MNRAS, 318, 879
Kaspi S., Smith P. S., Netzer H., Maoz D., Jannuzi B. T., Giveon U., 2000, ApJ, 533, 631
Kelly B. C., Treu T., Malkan M., Pancoast A., Woo J.-H., 2013, ApJ, 779, 187

Körding E. G., Migliari S., Fender R., Belloni T., Knigge C., McHardy I., 2007, MNRAS, 380, 301

Kormendy J., Ho L. C., 2013, ARA&A, 51, 511

Lohfink A. M., Reynolds C. S., Miller J. M., Brenneman L. W., Mushotzky R. F., Nowak M. A., Fabian A. C., 2012, ApJ, 758, 67

McHardy I. M., 2013, MNRAS, 430, L49

McHardy I. M., Papadakis I. E., Uttley P., Page M. J., Mason K. O., 2004, MNRAS, 348, 783

McHardy I. M., Gunn K. F., Uttley P., Goad M. R., 2005, MNRAS, 359, 1469

McHardy I. M., Koerding E., Knigge C., Uttley P., Fender R. P., 2006, Nature, 444, 730

McLure R. J., Dunlop J. S., 2001, MNRAS, 327, 199

Marconi A., Risaliti G., Gilli R., Hunt L. K., Maiolino R., Salvati M., 2004, MNRAS, 351, 169

Matt G., 2002, R. Soc. Lond. Philos. Trans. Ser. A, 360, 2045

Matt G. et al., 2014, MNRAS, 439, 3016

Miniutti G., Ponti G., Greene J. E., Ho L. C., Fabian A. C., Iwasawa K., 2009, MNRAS, 394, 443

Moran E. C., Eracleous M., Leighly K. M., Chartas G., Filippenko A. V., Ho L. C., Blanco P. R., 2005, AJ, 129, 2108

O'Neill P. M., Nandra K., Papadakis I. E., Turner T. J., 2005, MNRAS, 358, 1405

Onken C. A., Ferrarese L., Merritt D., Peterson B. M., Pogge R. W., Vestergaard M., Wandel A., 2004, ApJ, 615, 645

Papadakis I. E., 2004, MNRAS, 348, 207

Peterson B. M. et al., 2004, ApJ, 613, 682

Peterson B. M. et al., 2005, ApJ, 632, 799

Ponti G., Papadakis I., Bianchi S., Guainazzi M., Matt G., Uttley P., Bonilla N. F., 2012, A&A, 542, A83

Reines A. E., Greene J. E., Geha M., 2013, ApJ, 775, 116

Thornton C. E., Barth A. J., Ho L. C., Rutledge R. E., Greene J. E., 2008, ApJ, 686, 892

Thornton C. E., Barth A. J., Ho L. C., Greene J. E., 2009, ApJ, 705, 1196

Uttley P., McHardy I. M., 2005, MNRAS, 363, 586

Vaughan S., Edelson R., Warwick R. S., Uttley P., 2003, MNRAS, 345, 1271

Vaughan S., Iwasawa K., Fabian A. C., Hayashida K., 2005, MNRAS, 356, 524

Vestergaard M., 2002, ApJ, 571, 733

Vestergaard M., Peterson B. M., 2006, ApJ, 641, 689

Walton D. J., Nardini E., Fabian A. C., Gallo L. C., Reis R. C., 2013, MNRAS, 428, 2901

Xiao T., Barth A. J., Greene J. E., Ho L. C., Bentz M. C., Ludwig R. R., Jiang Y., 2011, ApJ, 739, 28

Zhou X.-L., Wang J.-M., 2005, ApJ, 618, L83

This paper has been typeset from a TEX/LATEX file prepared by the author.